Experiments in Fluids 30 (2001) 705–722 © Springer-Verlag 2001

Dynamics of hairpin vortices generated by a mixing tab in a channel flow

W. Yang, H. Meng, J. Sheng

Abstract To better understand mixing by hairpin vortices, time-series particle image velocimetry (PIV) was applied to the wake of a trapezoidal-shaped passive mixing tab mounted at the bottom of a square turbulent channel ($Re_h = 2{,}080$ based on the tab height). Instantaneous velocity/vorticity fields were obtained in sequences of 10 Hz in the tab wake in the center plane (x–y) and in a plane (x–z) parallel to the wall. Periodically-shed hairpin vortices were clearly identified and seen to rise as they advected downstream. Experimental evidence shows that the vortex-induced ejection of the near-wall viscous fluid to the immediate upstream is important to the dynamics of hairpin vortices. It can increase the strength of the hairpin vortices in the near tab region and cause generation of secondary hairpin vortices further downstream when the hairpin heads are farther away from the wall. Measurements also reveal the existence of a type of new secondary vortice with the opposite-sign spanwise vorticity. The distribution of vortex loci in the x–y plane shows that the hairpin vortices and the reverse vortices are spatially segregated in distinct layers. Turbulence statistics, including mean velocity profiles, Reynolds stresses, and turbulent kinetic energy dissipation rate distributions, were obtained from the PIV data. These statistical quantities clearly reveal imprints of the identified vortex structures and provide insight into mixing effectiveness.

Received: 24 February 2000/Accepted: 24 October 2000

W. Yang, H. Meng (✉)
Laser Flow Diagnostics Laboratory
Department of Mechanical and Aerospace Engineering
SUNY, Buffalo, NY 14260-4400, USA
E-mail: huimeng@eng.buffalo.edu

J. Sheng
Department of Mechanical Engineering
Johns Hopkins University
Baltimore, MD 21218, USA

The majority of this work was conducted when the authors were at Kansas State University, Department of Mechanical and Nuclear Engineering. This research was supported in part by an NSF CAREER award, grant number CTS-9625306. The generous supply of the mixing tab flow facility by Chemineer, Inc. is greatly appreciated. The authors wish to thank R.J. Adrian, C.R. Smith, and J. R. Sonnenmeier for helpful suggestions.

1 Introduction

A surface-mounted, inclined trapezoidal tab is known to shed hairpin-like vortices and thus can be used as a vortex generator to artificially create a turbulence-like flow to enhance mass and heat transfer (Gretta and Smith 1993). One example of its application is the high efficiency vortab (HEV) static mixer (Chemineer, Inc.), which consists of an array of such tabs mounted on the inner wall of a pipe or a duct (Fig. 1). Such static mixers are employed in the process industry for their high mixing efficiency and low pressure drop. Using flow visualization and anemometry techniques, Gretta and Smith (1993) studied flow characteristics of the wake of such a passive mixing tab in a water channel. They suggested that the wake of the tab comprised a pair of counter-rotating, streamwise vortices enveloped by a periodic sequence of hairpin-like vortices shed from the tab (Fig. 2). They identified footprints of hairpin vortices in the near-tab wake on the mean velocity profiles, which developed into a logarithmic law-of-the-wall type of behavior downstream, closely mimicking the behavior of a turbulent boundary layer. They also observed amalgamation or coalescence of the hairpin vortices, which was perceived as the reason for rapid growth of the mixed region. Elavarasan and Meng (2000) used planar laser induced fluorescence (PLIF) to visualize the coherent structures in the wake of a trapezoidal mixing tab. They found that the hairpin vortices and the pressure-driven counter-rotating vortex pair (CVP) persisted for different downstream distances in the wake and played different roles in mixing, and that the hairpin vortices dominated the majority of the wake. Detailed dynamics of the hairpin structures, however, are lacking in the past research of the mixing tab wake.

It is widely believed that the hairpin vortex, first identified by Theodorsen (1952), is a fundamental coherent structure in turbulent boundary layers (see, for example, Head and Bandyopadhyay 1981; Perry and Chong 1982; Moin et al. 1986; Kim 1987; Acarlar and Smith 1987a, b; Robinson 1990, 1991; Smith et al. 1991; Smith and Walker 1995; Haidari and Smith 1994; Peridier et al. 1991a, b; Smith and Walker 1995; Zhou et al. 1999). Using smoke visualization, Head and Bandyopadhyay (1981) were among the first to actually observe hairpin vortices in a fully developed turbulent boundary layer. They studied a zero-pressure-gradient turbulent boundary layer over a range of Reynolds numbers and found that the boundary layer consisted of elongated horseshoe/hairpin vortices inclined to the wall at approximately 45°. Perry and Chong (1982) extended Head and Bandyopadhyay's (1981) con-

Fig. 1. Kenics HEV static mixer maximizes the conversion of turbulent energy into efficient mixing. HEV units can be configured to square, rectangular, three-sided ducts, or open channels typically found in water treatment systems (www.chemineer.com/hev2.shtml)

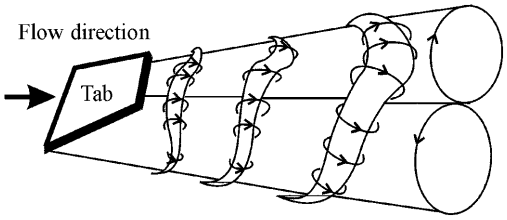

Fig. 2. A conceptual model of three-dimensional flow structures in the wake of a tapered, symmetric mixing tab proposed by Gretta and Smith (1993), with periodically shed hairpin vortices and a pair of counter-rotating vortices

clusion and suggested that turbulent boundary layers were comprised of hierarchies of interacting "young" and "old" hairpins originating from the wall. Robinson (1990) refined the picture of hairpin vortices through detailed study of direct numerical simulation (DNS) of a low-Reynolds-number turbulent layer and proposed that the three-dimensional hairpin vortices were mostly asymmetric in shape. A comprehensive review of hairpin vortices and other coherent structures in the turbulent boundary layer was given by Robinson (1991).

Hairpin vortices may be generated artificially in laminar boundary layers in order to gain understanding of their dynamics in turbulent boundary layers. For example, through localized disturbances by injection/suction, hairpin vortices were generated in a laminar axisymmetric rotating shear flow by Malkiel et al. (1999), and their dynamics was examined using laser Doppler velocimetry (LDV), particle image velocimetry (PIV), and flow visualization techniques. Furthermore, a series of "kernel" experiments on hairpin vortices were conducted at Lehigh University (see Acarlar and Smith 1987a, b; Smith et al. 1991; Haidari and Smith 1994; Smith and Walker 1995). These studies were aimed at discerning a basic fluid mechanical process (hairpin vortex dynamics in this case) that is relevant to the turbulent boundary layer. Acarlar and Smith (1987a) studied the steady formation of a continuous stream of hairpin vortices in a laminar boundary layer behind a hemispherical bump, while Haidari and Smith (1994) generated a single hairpin vortex by impulsive local injection of fluid from the surface. These mechanisms for generating hairpin vortices were, in a sense, similar to that of the mixing tab studied by Gretta and Smith (1993). The low-speed surface fluid was displaced by injected fluid or solid protuberance, causing an unstable shear layer that rolled up into a hairpin. Haidari and Smith (1994) further observed development of new hairpin vortices from the initial hairpin vortex through (i) the deformation of the vortex lines comprising the initial hairpin and (ii) a process of vortex–wall interaction. The second mode of hairpin regeneration was rather intriguing: the interaction of the primary vortex (essentially inviscid) with the surface (viscous layer) caused sharp eruption or ejection of low-speed surface fluid, which subsequently interacted with the outer flow and gave rise to a secondary hairpin vortex. Peridier et al. (1991a, b), through their in-depth study of vortex-induced boundary-layer separation, coined this mechanism as "viscous–inviscid interaction", which is one example of the parent–offspring type of hairpin vortex regeneration mechanism (Smith and Walker 1995).

From detailed PIV experimental measurements, Meinhart and Adrian (1995a) observed a train of hairpin vortices in a natural turbulent boundary layer. Consistent with their observations, Zhou et al. (1997) and Zhou et al. (1999) studied the evolution of a single hairpin-like structure in the turbulent wall layer in a channel flow by DNS. They showed that the hairpin structure was capable of generating a coherent packet of subsequent hairpins through an auto-generation process and proposed that formation of secondary hairpin vortices was caused by the viscous reconnection of its parent hairpin legs. Their observation of the mechanism was based on careful three-dimensional visualization of simulated vortex structure that had not been available experimentally.

In addition to the two parent–offspring scenarios mentioned above, in which a parent vortex spawns offspring vortices by direct induction, a number of mechanisms based on instabilities (e.g., centrifugal and wave shear instabilities, direct resonance, streak instability) have also been proposed for the turbulent boundary layer (see Schoppa and Hussain 1997). In these mechanisms new vortices are spawned by an unstable base flow, where existing vortices play only an indirect role via feedback. The instability-based mechanisms appear to be related mostly to streamwise vortices.

In the current study, we used PIV to study hairpin vortices in the wake of a passive mixing tab mounted at the bottom of a square channel. This study was primarily motivated by the need for developing fundamental understanding and ultimately design rationales for the tab-based mixers. As in the work of Gretta and Smith (1993) and Elavarasan and Meng (2000), the tab in the current experimental study was designed to emulate a tab element in a typical HEV mixer. There were three objectives to this study: (i) to gain insight into the dynamics and regeneration of the hairpin vortices in the tab wake from the detailed time-series velocity and vorticity fields, (ii) to assess quantitatively turbulent mixing by the tab by evaluating turbulent characteristics obtained from a large quantity of PIV realizations, and (iii) to gain insight into the mixing mechanism from the relationship between turbulence statistics and dynamics of the hairpin structures.

Since their sizes were comparable to the boundary-layer thickness of the duct flow, the hairpin vortices in the tab

wake were not directly comparable to those formed inside a natural turbulent boundary layer. However, since all hairpin vortices share some basic topological and dynamical characteristics, we believe that hairpin vortices generated in the tab wake could serve as a model experiment that would help us to further understand the evolution, regeneration, and interaction of hairpin structures in general, including those in a natural turbulent boundary layer. This model experiment offers the advantage of large-size structures and slow evolution suitable for time-resolved PIV study, as well as a controlled environment with negligible background turbulence influence.

The application of time-series PIV measurements to hairpin vortex dynamics clearly offered an advantage over flow visualization employed by Gretta and Smith (1993) and Elavarasan and Meng (2000). It is well known that the dynamics of a scalar (such as dye concentration) cannot faithfully represent vortex dynamics, primarily due to the absence of the vortex-stretching mechanism. Since vortex structures are inherently related to the coherent vorticity distribution, quantitative full-field measurements of the velocity and vorticity fields are essential to exploring the topology and dynamics of hairpin vortices. However, to compensate for the limited temporal resolution and the lack of cross-stream plane imaging capability of our current PIV system, the current study was carried out simultaneously with a PLIF visualization experiment in a similar flow configuration as described by Elavarasan and Meng (2000). In the PLIF experiment, the hairpin evolution was recorded at the normal video frequency (30 f/s vs. 10 f/s for the PIV), and all three planes (x–y, x–z, and y–z) in the tab wake could be imaged. These helped to obtain a more comprehensive picture of the three-dimensional topology of the structures. By changing the position of the cross-stream illumination plane (y–z) progressively downstream, streamwise vortices were clearly visualized in the PLIF images.

Results of PLIF revealed that the large counter-rotating vortex pair (CVP), generated due to the pressure difference before and after the tab, did not persist very far downstream. Typically they lasted only 1.5 to 2 tab heights downstream, depending on the Reynolds number. After the CVP was "gone" the flow was only dominated by the hairpin structures, which could still be seen at 12 tab heights downstream. This observation was a major deviation from Gretta and Smith's model (1993) shown in Fig. 2.

Besides using a different experimental tool, the PIV experiment described in the current work also differed from the PLIF experiment in the base flow conditions: a developing turbulent channel flow at a Reynolds number based on the tab height of $Re_h = 2{,}080$ in the PIV study versus a laminar flow over a flat plate where Re_h varied from 450 to 2,100 in the PLIF study. However, cross-checking the results from the two experiments revealed many similarities between the two flows; therefore it is instructive for us to refer to the PLIF results from time to time.

2 Experimental setup

2.1 Test flow setup

The PIV measurements of a mixing tab wake were conducted in a closed Plexiglas square channel system supplied by Chemineer Inc. The water channel system had a total dimension of 123 × 7.62 × 7.62 cm with double inlets and outlets 2.4 cm in diameter oriented at 90° on the side walls (Fig. 3). Water flow was gravity-fed by a 2.7-m water head from a 15-gallon reservoir. The flow entered though the

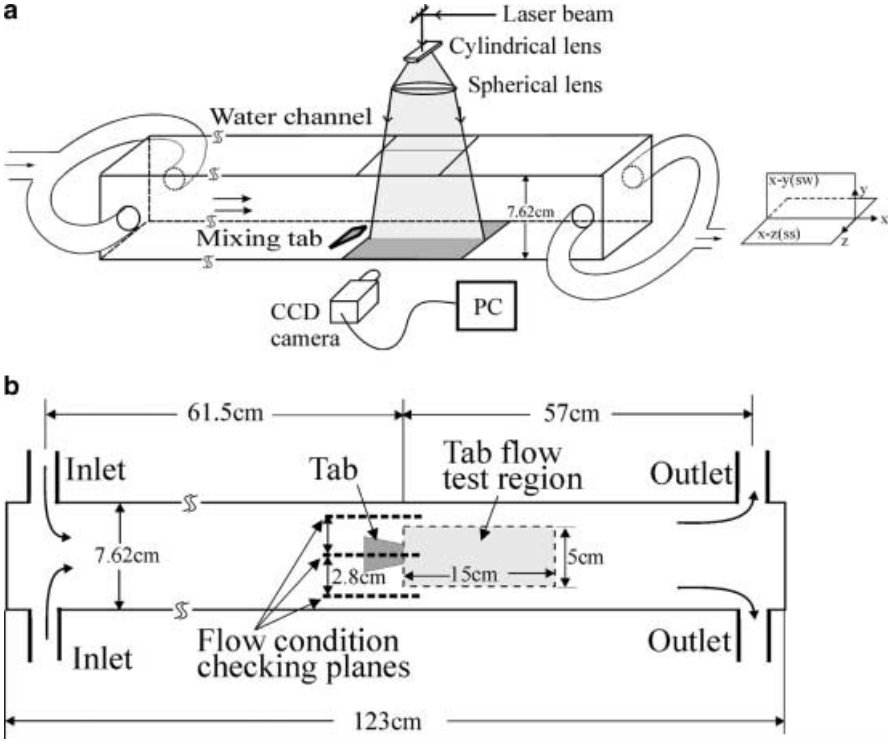

Fig. 3a, b. Experimental setup. **a** The water channel was illuminated by a laser light sheet at the center plane of the tab (the x–y plane). For measurements of the x–z plane, the light sheet was horizontal, 1.9 cm away from the channel bottom, and the camera was mounted vertically. **b** Top view of the channel with dimensions

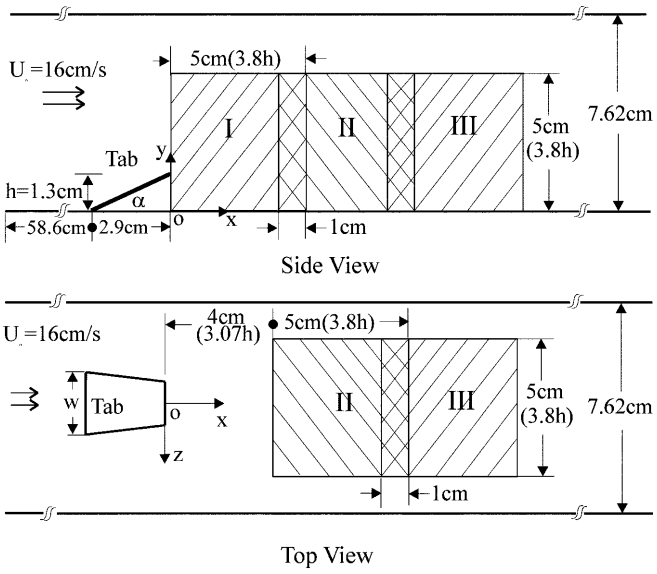

Fig. 4. Schematic of the mixing tab geometry and PIV measurement windows. $\alpha = 24.5°$, $h = 1.3$ cm, $w = 2.2$ cm

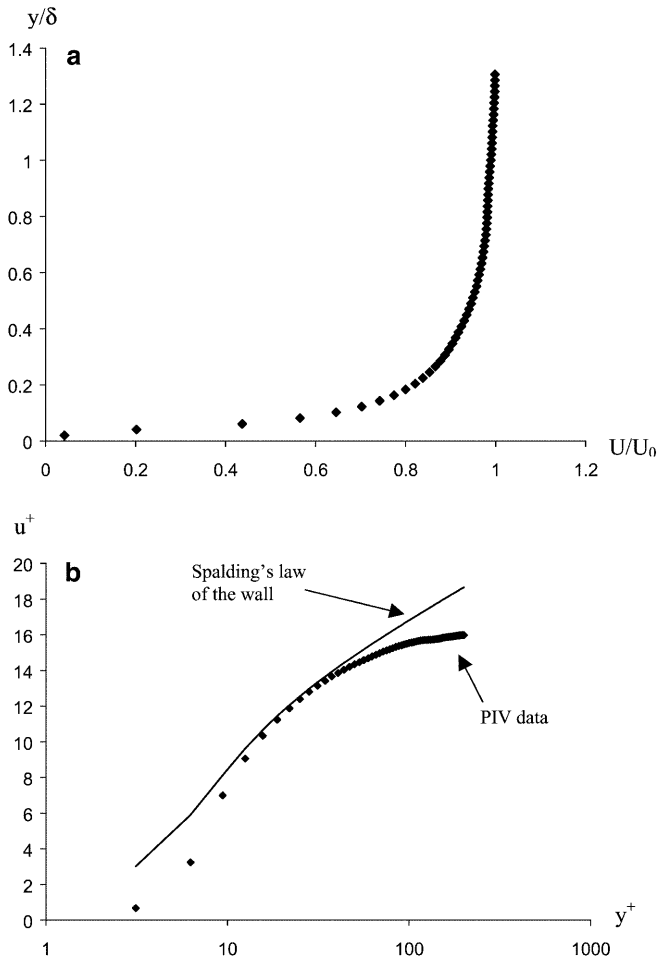

Fig. 5a, b. Mean streamwise velocity profile at 61.5 cm from inlets in absence of the tab. When the tab was mounted, the tab tip would be at this location and the tab height (h) would correspond to $y/\delta = 0.85$, where δ is the boundary-layer thickness based on $0.99U_0$. The profile was averaged from 1,120 instantaneous profiles measured by PIV. **a** Scaled with outer variable δ and U_0 and **b** scaled with inner variables ($y^+ = y/y^*$ and $u^+ = U/u^*$). The *solid line* was calculated from Spalding's law of the wall

double inlets and formed opposing jets, which collided with each other and formed a developing channel flow downstream. No flow conditioning was employed in the channel system. This experimental rig was designed to mimic a real HEV mixer used in industry except that only a single tab was included. A symmetric tapered mixing tab was mounted at the center of the bottom surface of the channel with the tip at 61.5 cm (25.6 inlet diameters) from the center of inlets. The geometry of the tab is shown in Fig. 4, where $\alpha = 24.5°$, $h = 1.3$ cm, $w = 2.2$ cm. The free-stream flow velocity (U_0) was 16 cm/s, which corresponds to a Reynolds number, $Re = 1.21 \times 10^4$, based on the channel height, and $Re_h = 2{,}080$, based on the tab height (h).

The flow conditions without the tab were checked with PIV measurements in three vertical planes at spanwise positions of $z = 0$, 2.8 and −2.8 cm (Fig. 3). To obtain velocity profiles over the full channel height, the windows for these PIV measurements were 7.62×7.62 cm in size, starting at 55.0 cm (42.3 h) and ending at 62.6 cm (48.2 h) from the inlet center. To ensure stable turbulence statistics, 1,120 PIV realizations were taken at each spanwise location.

Results of the mean velocity profiles $U(x,y)$ in all three planes show that the two-dimensionality of the channel flow was achieved reasonably well in the region of the tab. The average difference in U for the same (x,y) coordinates across different spanwise planes was found to be 5.1% of U_0. The off-center planes were located outside the measurement region for the tab wake. Hence the spanwise uniformity of the channel flow in the test region was ensured.

Careful examination of the velocity profiles in the center plane reveals that the channel flow was still developing downstream in the tab region of our interest. In order to resolve the boundary-layer profiles on the center plane near the bottom wall, another measurement was made by zooming in the PIV camera to record a 2×2 cm region starting 59.6 cm from the channel inlets with a spatial resolution of 0.31 mm in the x and y directions. From 1,120 PIV realizations, the mean velocity field was obtained for the 2×2 cm region and found to be consistent with the results for the 7.62×7.62 cm region. Over the 2 cm test window length the boundary-layer thickness (δ) based on $0.99U_0$ increased from 1.31 to 1.53 cm. Figure 5 shows the boundary-layer profile at $x = 61.5$ cm (the location of the tab tip) from the inlet center. At this location the boundary-layer thickness δ was 1.53 cm (or 1.18h). Figure 5a gives the profile scaled with the outer variables U_0 and δ. To further compare the developing boundary-layer profile with the fully developed turbulent boundary-layer profile, we plot the measured boundary-layer profile scaled with the inner variables in Fig. 5b and compare it with the Spalding's law-of-the-wall equation for smooth pipe flows, $y^+ = u^+ + e^{-\kappa B}\left[e^{-\kappa u^+} - 1 - \kappa u^+ - \frac{(\kappa u^+)^2}{2} - \frac{(\kappa u^+)^3}{6}\right]$, where $\kappa = 0.4$ and $B = 5.5$ (Spalding 1961). Here the wall shear stress $\tau_w = 0.1$ N/m^{2}was estimated by curve-fitting the last three data points next to the wall. From the comparison, the measured boundary profile agreed well with Spalding's law of the wall between

$y^+ \approx 10$ and $y^+ \approx 40$ but deviated from it at the two ends. The deviation close to the wall was likely caused by the PIV measurement errors. This is because: (1) the strong light reflection from the wall introduced noise in PIV images, (2) the velocity of the seeding particles at the near-wall region was so small ($\sim$0.016 m/s) that the uncertainty of PIV measurement could not be ignored (for details of uncertainty analysis, see later section). At $y^+ > 40$ we do not expect significant measurements errors were negligible, and the deviation from Spalding's profile indicates that the flow was not fully developed.

The boundary layer at the upper wall was slightly thicker than at the bottom wall, but it was sufficiently far from the tab such that it would not have a significant influence on the dynamics of the flow generated by the tab. The free-stream turbulence intensity decreased from 8 to 7% across the test window in the downstream direction.

Throughout the rest of this paper, PIV measurements with the tab will be discussed and all distances will be referenced to the tab tip location at the wall (point O in Fig. 4) and often non-dimensionalized by the tab height, h, where $h = 1.3$ cm.

2.2
PIV experimental setup

As illustrated in Fig. 3, the test section was illuminated with a 0.5-mm thick laser light sheet. The light sheet consisted of a series of double pulses separated by a brief time lapse and were produced by a pair of digitally sequenced Nd: YAG lasers (Spectra-Physics PIV 400) operating at 10 Hz. The light sheet optics included a cylindrical lens, a 500-mm focal length spherical lens, and several reflecting mirrors. The spherical lens was used to confine the light sheet to a uniform thickness within the test section. The flow system was filled with distilled water that was fully seeded with hollow glass particles (TSI 10089) of nominal diameter 8–12 μm and specific density 1.05–1.15 at a concentration of approximately 50–60 particles/mm^3. Time-series PIV image pairs formed by 90° side scattering of the seeding particles are recorded by a digital CCD camera (Kodak ES 1.0) at a resolution of 1008×1018 pixels. The images were transferred to the host PC memory via a PCI bus-based frame grabber (Data Translation DT3157) and finally saved on the hard disk of the host PC. The PIV system had the capability of acquiring double images at a 10 Hz repetition rate. Due to limited computer memory and data transfer rate between the computer memory and the hard disk, for each data acquisition, only 27 pairs of PIV images are recorded continuously within a 2.7-s period with a 0.1-s interval. The timing of the double-laser pulses and operation of the electronic shutter on the CCD camera were synchronized with a digital function generator. To optimize the displacement of particle pairs between the double exposures to improve measurement accuracy, the time lapse between the double pulses was adjusted depending on the mean displacement in the test section.

The signal-to-noise ratio of the PIV images was optimized through: (1) suppressing the background noise by reducing the light sheet thickness and hence reducing the number of de-focused particles in PIV images, (2) producing a uniform intensity and thickness of the light sheet within the CCD camera viewing area, and (3) covering the bottom of the channel in the test section by a high-temperature black paint to reduce optical noise by reflection. The reflections were found to be responsible for generating "bad" vectors in the PIV measurements in the near-surface region.

Based on a compromise between the requirements of recording a large field of view and resolving detailed flow structures, the viewing area of the PIV system was chosen to be 5×5 cm ($3.8\ h \times 3.8\ h$). PIV measurements in three partially overlapping regions (adjacent imaging regions overlap by 1 cm or 0.77 h) starting from the tip of the tab aligned with the spanwise center of the tab, marked as regions I, II, and III in Fig. 4. These were chosen since we have observed that the hairpin vortices were most active in these regions. The plane defined by these regions hereafter is referred to as the streamwise/wall-normal (SW) plane or the x–y plane. A total of 216, 189, and 162 instantaneous PIV realizations were recorded in regions I, II, and III, respectively. In addition, in a horizontal plane $1.46h$ (1.9 cm) from the channel bottom, hereafter referred to as the streamwise/spanwise (SS) plane or x–z plane, 216 and 243 PIV realizations were also recorded in two partially overlapping regions, regions II and III, respectively.

2.3
PIV data processing

During the processing of the PIV images, we used a sliding window to select an interrogation cell (IC) of 64×64 pixels. The average displacement for the particle pairs in each IC was calculated using a multi-pass and multi-resolution cross-correlation algorithm with the standard Gaussian fit sub-pixel technique, which has been widely adopted in PIV processing algorithms (Raffel et al. 1998). After one IC was processed, the window was shifted 20 pixels to process the next IC, resulting in 50% overlapping. The process was repeated until the whole image pair was covered. In this way, each PIV realization provided 50×50 or 2500 instantaneous velocity vectors. The spatial resolution of the vectors was 1.0 mm. Our correlation algorithm benefited from the use of heuristic selection of the correlation peak, which drastically cut down the number of "bad" vectors (less than 5%). The PIV data processing software was implemented on a Windows NT 32-bit platform running on a pentium PC. Before taking any PIV measurement data for the experiment, the whole system was calibrated by measuring the velocity vector field of a rotating sand disk and simulated particle field.

The accuracies of PIV measurements (including velocity, vorticity, and turbulence prosperities) ultimately depend on the uncertainty of the particle displacement measurements. When a correlation technique with sub-pixel peak detection is used, the displacement accuracy is affected by particle image diameter, background noise, particle image density, particle image shift, and out-of-plane motion (Raffel et al. 1998). In the current experiment, we optimized the particle image size (1–4 pixels) and seeding densities (50–60 particles/mm^3) to secure valid detection of correlation peak. Under these conditions, the uncertainty resulting from these two factors was

roughly 0.06 pixels. Including the remaining factors, the uncertainty in the displacement measurements was estimated to be in the order of 0.1 pixels. In fact, 0.1 pixel is now a commonly accepted uncertainty value for standard cross-correlation-based sub-pixel PIV processing techniques (Keane and Adrian 1992).

With the double-pulse separation of 5 ms, a displacement uncertainty of 0.1 pixels translates to an uncertainty of $e \approx 1.0 \times 10^{-3}$ m/s in velocity, which was 0.6% of the free-stream velocity. The uncertainty in Reynolds stresses and kinetic energy was then $2ue \approx 2 \times 0.16 \times 10^{-3} = 3.2 \times 10^{-4}$ m^2/s^2, or $2ue/u^2 = 2e/u \approx 1.2\%$ relative to the free-stream velocity. The uncertainty in vorticity was $4e/\Delta x = 4 \times 10^{-3}/0.002 = 2$ s^{-1} (Δx is the grid size), which was 4.4% of the peak vorticity magnitude in the vortex structures in the tab wake.

3
Results and discussion

3.1
Vortex identification, hairpin signature and vortex strength

The existence of hairpin vortices in the tab wake has been established by Gretta and Smith (1993) and Elavarasan and Meng (2000). To study detailed hairpin vortex dynamics using PIV, however, a reliable method to identify and track vortex structures from the two-dimensional PIV data is still needed.

A number of techniques have been proposed to identify vortices (Zhou et al. 1999; Jeong and Hussain 1993; Chong et al. 1990; Kim 1987) with varying success and limitations under different situations. For two-dimensional PIV measurements, we find that a simple method that combines the moving-frame velocity field and vorticity magnitude works rather well for identifying vortex structures in the PIV data. According to Robinson's (1991) working definition for vortex identification (which has often been applied to PIV measurements in the past), a vortex exists when instantaneous streamlines mapped onto a plane normal to the vortex core exhibit a roughly circular or spiral pattern, when viewed from a reference frame moving along with the center of the vortex core. The question then is how to determine the velocity of an appropriate reference frame. Frequently this is determined through a trial-and-error procedure by visually inspecting which value of velocity, when subtracted from the measured velocity field, gives the most obvious vortex structure. A drawback of this approach is that it cannot simultaneously locate multiple vortices that advect at different speeds. Meinhart and Adrian (1995) coped with this problem by subtracting different percentages of free-stream velocity for structures in different layers. However, even in the same layer, vortex structures may travel at different speeds. To reduce the effort of the trial-and-error procedure, and to be informed of all possible vortex structures in the same field of view, we add the vorticity field as an indication to help in locating the vortices. Since the vorticity field is Galilean invariant, multiple vortices manifest themselves simultaneously as regions of concentrated correlated high vorticity packets. Vorticity alone cannot indicate a vortex. A strong shear layer, for example, is associated with high vorticity but is not a vortex. Therefore, a combination of the reference-frame method and the vorticity-magnitude method provides a more reliable and practical way to identify vortex structures from PIV measurements.

If the reference frame is properly chosen, the velocity field on the streamwise/wall-normal plane cutting through a hairpin structure manifests certain characteristics that are attributed as the hairpin signature (Zhou et al. 1997). Such a signature (Fig. 6a) includes elements such as: roughly circular motion associated with the hairpin head, low-momentum ejection below the head (Q2, i.e., second quadrant of the u–v plane, identified in Fig. 6a), a shear layer inclined from the wall at roughly 45°, and a low-speed region below the ejection. Here Q2 refers to the direction pointing outward in the second quadrant. An important implication of the signature, consistent with the three-dimensional topology and dynamics of the hairpin vortex, is that the entire hairpin vortex collectively induces a strong upward and backward fluid pumping motion (ejection) below the hairpin head, and between the hairpin legs. By the same token, a hairpin signature for a streamwise/spanwise plane cutting through the hairpin legs can also be inferred: two pairs of counter-rotating vortex structures (common flow-in) with coarsely circular motion and a low-speed fluid region in between meeting the high-speed flow from upstream. This is illustrated in Fig. 6b.

As examples, we show several sets of time-series PIV measurements of the tab wake in region I of the x–y plane (Fig. 7), region II of the x–y plane (Fig. 8), and region II of the x–z plane (Fig. 9). The time lapse between consecutive pictures in each set was 0.1 s. With the indication of vorticity, an appropriate velocity was subtracted from each set of data. These two-dimensional cross-sections clearly

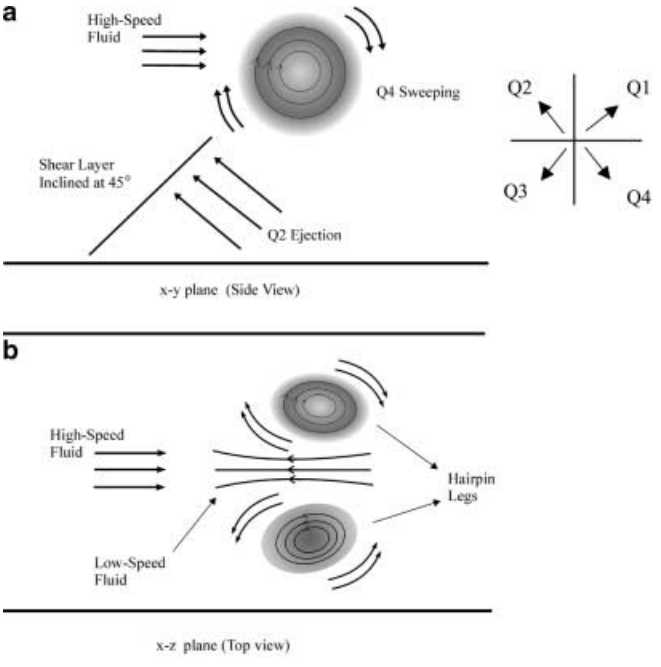

Fig. 6a, b. Hairpin vortex signatures in the tab wake **a** in streamwise/wall-normal (x–y plane and **b** in streamwise/spanwise (x–z) plane

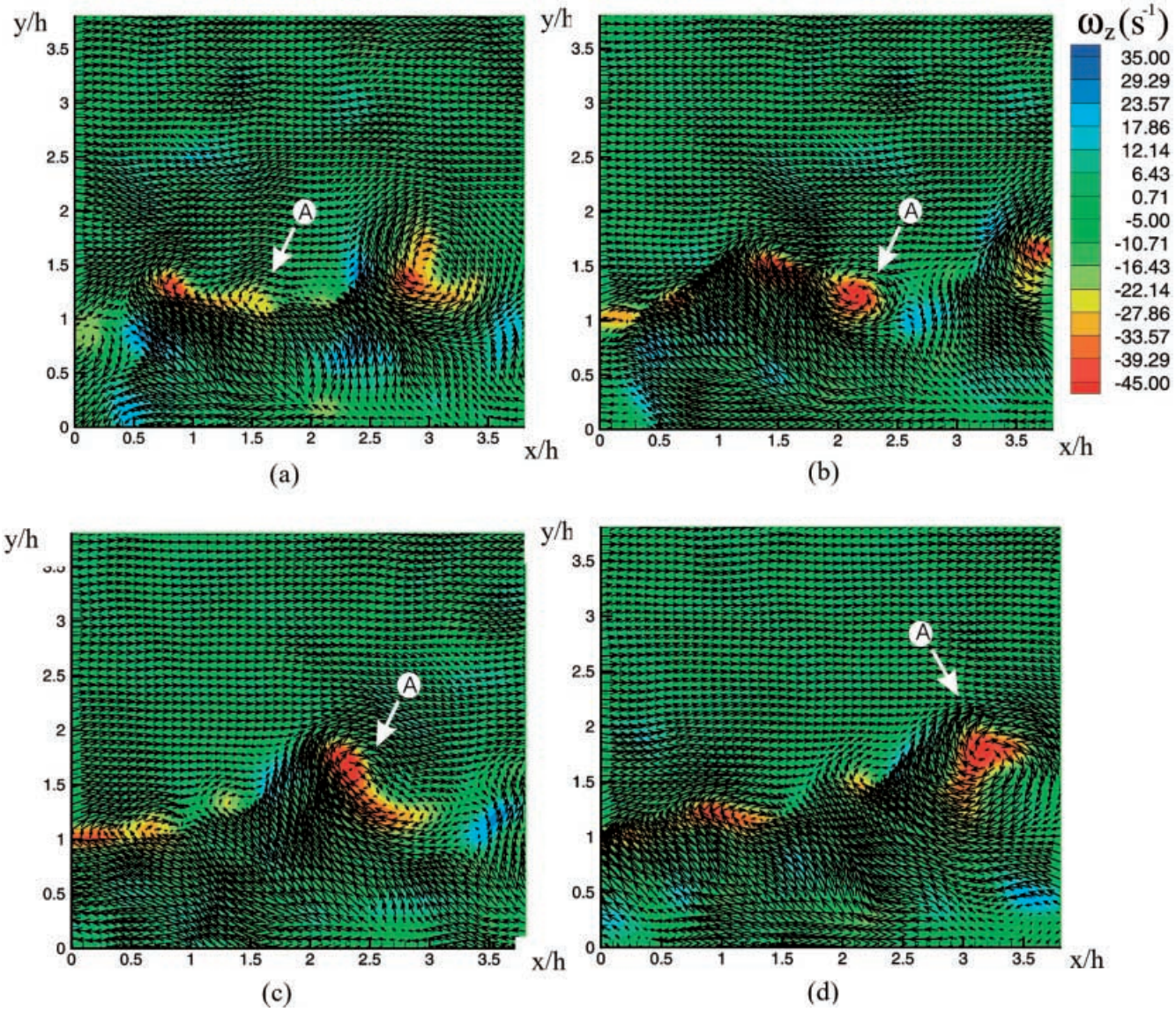

Fig. 7. A time series of instantaneous velocity fields (separated by 0.1 s and subtracted by 56% U_0) superimposed with their vorticity fields obtained in region I in the center x–y plane, showing evolution of the hairpin vortex head A. The *bar* shows the vorticity magnitudes

exhibited the hairpin vortex signatures. In the following sections we further discuss the dynamics of the hairpin vortices revealed from these pictures.

To calculate vortex strength the boundary of a vortex structure needs to be clearly defined. For this purpose, we resort to the vortex identification method of Jeong and Hussain (1993) based on regions of negative λ_2, the second largest eigenvalue of the tensor $S_{ik}S_{kj} + \Omega_{ik}\Omega_{kj}$, where S_{ij} and Ω_{ij} are the symmetric and antisymmetric parts of the tensor $\partial_i u_j$, respectively. Once the boundary is determined, the vortex strength can be calculated from area integration of vorticity. We tested this method with a numerically generated Oseen vortex field. The extracted circulation differed from the analytical solution by less than 0.1%. In absence of complete three-dimensional velocity field measurements, however, this method gives only a rough estimate of the vortex boundary and thus vortex strength. We used such estimates to provide statistical trends of the strength of hairpin vortices with respect to the downstream distance in the PIV measurement plane.

3.2
Initial development of hairpin vortices

Figure 7 shows a typical time series of instantaneous velocity fields on the x–z plane in region I, immediately downstream of the tab. A reference speed of 56% U_0 was subtracted from the velocity fields to visualize the vortices, and the calculated vorticity (ω_z) fields was superimposed onto the velocity maps, with red representing the negative vorticity and blue, the positive. In the first instant (Fig. 7a), after the flow passed the tab tip (at $x = 0$), flow separation due to the tab was evident. A clockwise-rotating vortex centered at $x \approx 3\ h$ was rolled up from a negative-vorticity shear layer (due to the tab tip) undergoing the Kelvin–Helmholz instability. Upstream at $x \approx 1.5\ h$ a new hairpin vortex (marked by

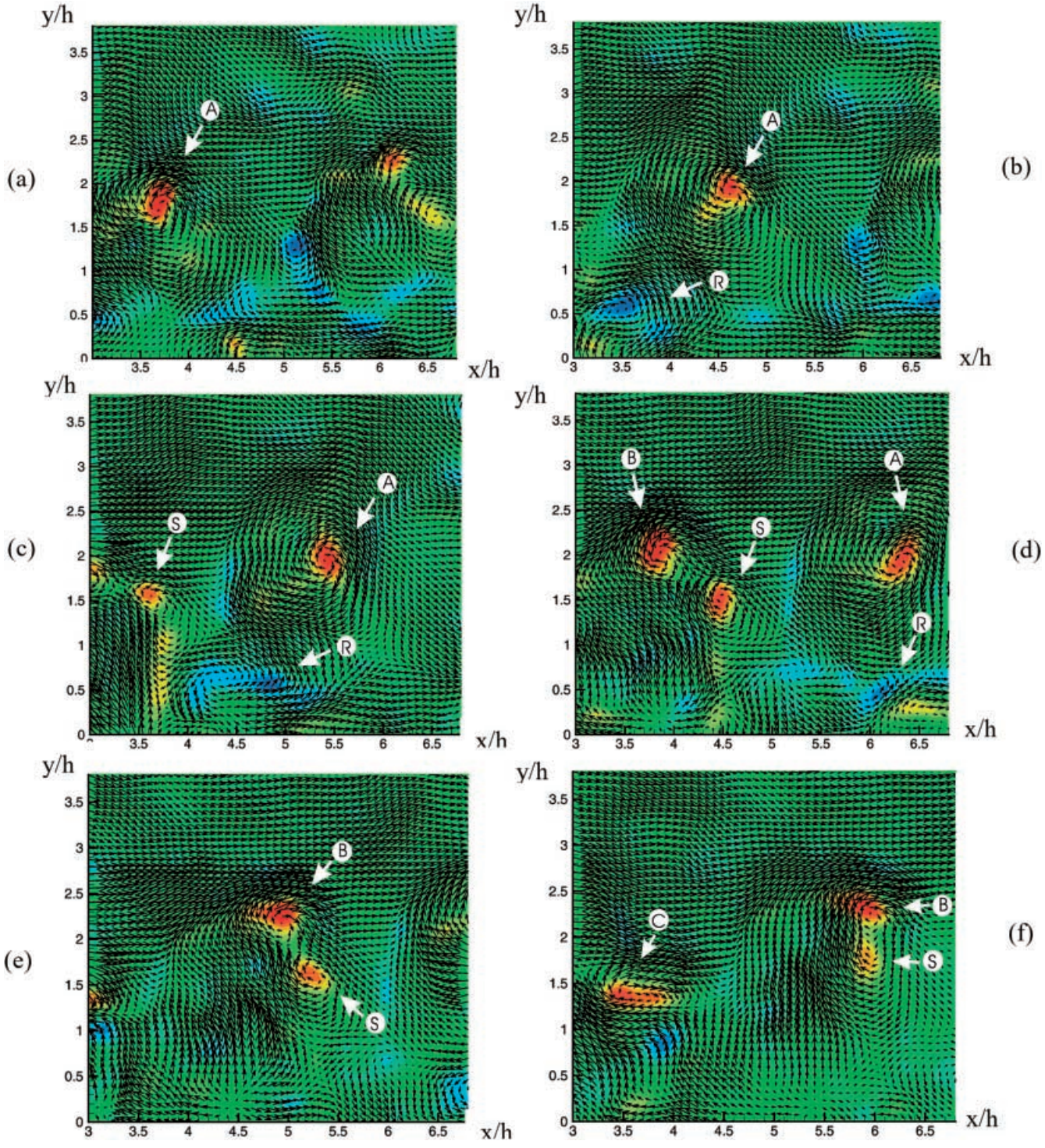

Fig. 8. A time series of instantaneous velocity fields (separated by 0.1 s and subtracted 56% of U_0) superimposed with their vorticity fields obtained in region II in the center x–y plane, demonstrating hairpin vortex regeneration and post-regeneration. A, B, and C are periodically-shed primary hairpin vortex heads. S is a secondary hairpin vortex head and R a reverse (opposite-sign) vortex, both produced by vortex A. For vorticity magnitudes, see *bar* in Fig. 7

the white arrow and A), now relatively small and weak, began to roll up. In the next instant (Fig. 7b), vortex head A was fully rolled up and became bigger and stronger. An additional packet of high-vorticity region upstream of A was attached to the hairpin vortex head A. In the subsequent instant (shown in Fig. 7b–d), this additional mass of fluid merged with vortex head A, and the resulting elongated vortex cross-section turned clockwise while continuing to rise.

The circulation of hairpin vortex head A was estimated, using Jeong and Hussian's (1993) vortex identification method, to be −0.0003, −0.0007, −0.0012, and −0.00105 m^2/s for Fig. 7a, b, c, and d, respectively. Hence, vortex A increased its strength while traveling down-

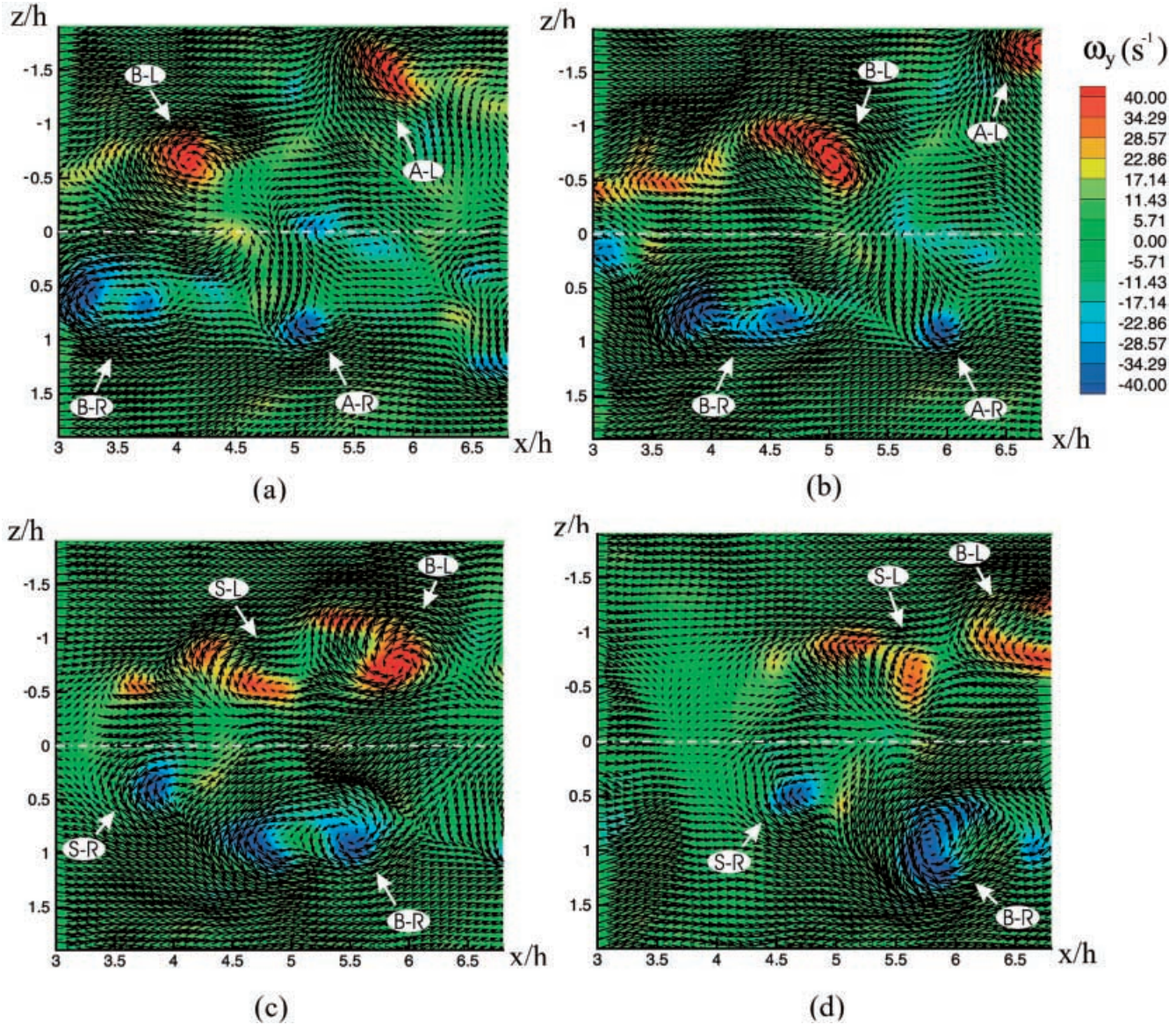

Fig. 9. A time series of instantaneous velocity fields, viewed with 50% U_0, superimposed with their vorticity fields obtained in region II in the x–z plane. Successive snapshots are separated by 0.1 s. A and B are two primary hairpin vortices and S a secondary hairpin vortex produced by vortex B. The letters L and R denote left and right leg, respectively

stream. To check if there was a general trend of increasing vortex strength with downstream distance at this stage, all the hairpin vortex heads measured in region I (a total of 431) were picked up by the vortex identification method and their circulations were calculated individually. Then region I was divided into four zones, each with a width of 0.95h, and the circulations of identified hairpin vortex heads were averaged within each zone. From the plotted average vortex strength (absolute value of circulation) versus x/h (Fig. 10), it is clear that the strength of hairpin vortex heads increased in the first three zones and then decreased in the last zone. Possible physical interpretations are given below:

1. The increase of vorticity magnitude of the marked vortex core A from Fig. 7a to Fig. 7b had to be caused by vortex stretching along the z-axis. Flow visualization of the y–z planes (Elavarasan and Meng 2000) indicated that, for

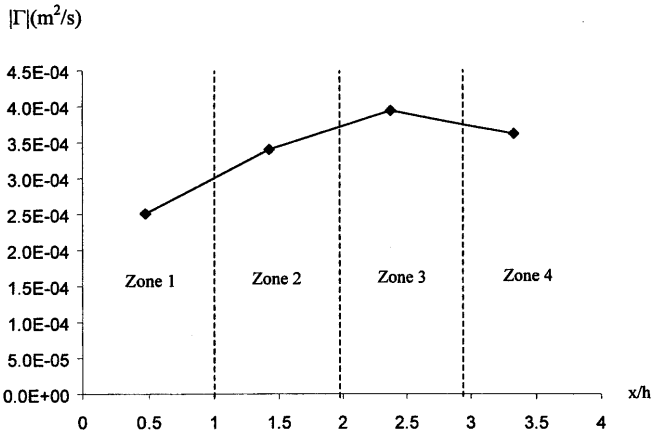

Fig. 10. Strength of hairpin vortex heads averaged in four zones in region I in the x–y plane as a function of the downstream distance

distances from 0 to 1.5h or from 0 to 2h downstream of the tab tip (depending on the Reynolds number), the flow was dominated by the CVP. It is expected that a developing hairpin head in region I would be located on top of the CVP, where the common-up ($v > 0$) fluid split into $w > 0$ flow and $w < 0$ flow in the cross-stream plane, causing the stretching of the hairpin arch along the z-axis. This explanation is sketched in Fig. 11a and supported by the PLIF picture at a plane approximately 0.5h downstream of the tab tip in Fig. 11b.

2. Although the vortex core size could increase as a result of entrainment or viscous diffusion, the sudden addition of a high-vorticity packet onto an existing vortex A at instant (b) had to be caused by a different mechanism. We postulate that this was related to the pumping (ejection) of the near-wall fluid, which carried boundary-layer vortex lines. When the ejected low-speed fluid interacted with the high-speed free-stream fluid, these vortex lines were organized and eventually attached to the hairpin head through viscous diffusion. Hence, the strength of the hairpin heads could increase at this stage. This concept is illustrated in Fig. 12.
3. Two mechanisms could contribute to the upward pumping of the low-speed fluid: the spiral motion of the CVP (common-up in the center), and the induction by the hairpin vortex. In the near-tab region, the CVP was the dominant cause, but with increasing downstream distance (beyond 2 h), the influence of CVP diminished and the hairpin vortices persisted further downstream and remained the source of pumping.
4. The phenomena of vortex-induced breakdown of near-wall flow and ejection of a packet of the near-wall viscous fluid to the immediate upstream appear to be important to the dynamics of hairpin vortices. In the example given above, this mechanism contributed to the augmentation of the strength of the hairpin vortices shortly after they were shed from the tab. Further downstream, when the hairpin heads were further away from the wall, this ejection could cause generation of secondary hairpin vortices.

By inspecting many time-sequences of PIV data taken in different regions of the tab wake, it was found that the vortex augmentation process was most significant between 1h and 3h downstream of the tab.

3.3 Lifting of hairpin vortices

To further examine the evolution of the vortex structures in the tab wake, we plot the loci of all vortices identified from the PIV measurements in the streamwise/wall-normal plane in two measurement regions, I and II, and show them in Fig. 13. Here attention should be focused on the circles distributed in the top layer. These circles represent the hairpin vortex heads. Other features of these plots will be discussed in later sections. It is evident that the hairpin vortex heads increased their heights with the downstream distance. They were lifted from the height of the tab at an average angle of 11° in region I and were concentrated to within a span of ~1 h width. After $x > 3.0h$ (in measurement window region II), the average lifting angle of the hairpin loci was reduced to 7°, and the zone span increased to ~2 h. The lifting of the hairpins can be attributed to an upward vertical velocity component induced by the strong common-up rotation of the CVP, which dominated until a downstream distance of 1.5–2 h, and by the hairpin legs, which took over thereafter.

Hairpin vortex heads could still be observed at 12h downstream of the tab in our PIV measurements, which suggests that hairpin vortices are long-lived vortices in the wake of a surface-mounted mixing tab even in a channel flow at a relatively high-Reynolds number.

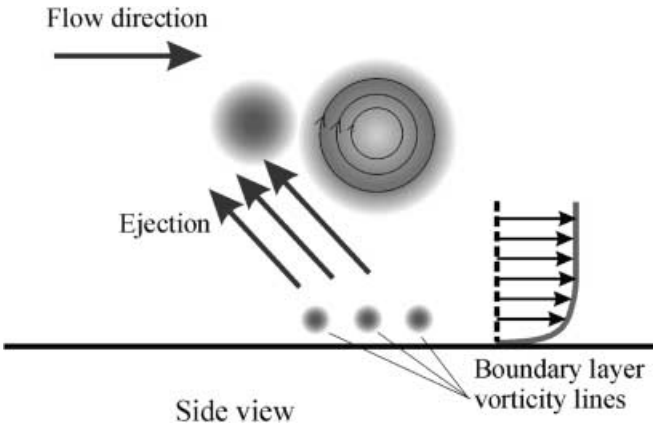

Fig. 12. Concept model for the augmentation of hairpin vortex head due to ejection of the boundary-layer vortex lines

3.4 Generation of new vortices

In the mid-field region of the tab wake, the hairpin vortices were lifted farther away from the wall than in the near-tab region. The PIV data revealed the existence of secondary vortices in this region. These secondary vortices were not shed from the tab, but were generated as a result of the dynamics of the primary hairpin vortices. Figure 8 shows a

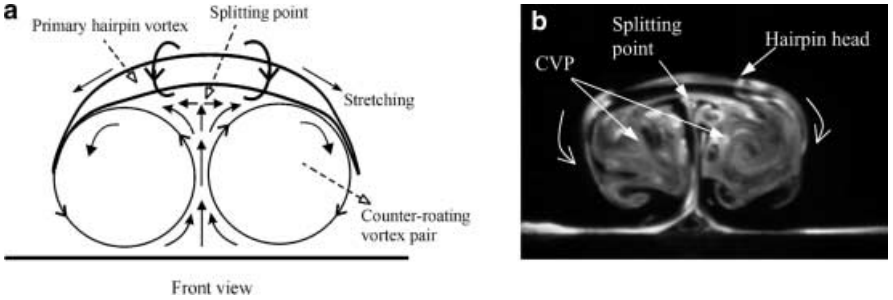

Fig. 11a, b. Stretching of hairpin vortex by the counter-rotating vortex pair (CVP) at the initial stage. The splitting point refers to the point where velocity $v \approx 0$ and $w \approx 0$. **a** Concept model and **b** PLIF visualization of a plane approximately 0.5h downstream of the tab tip

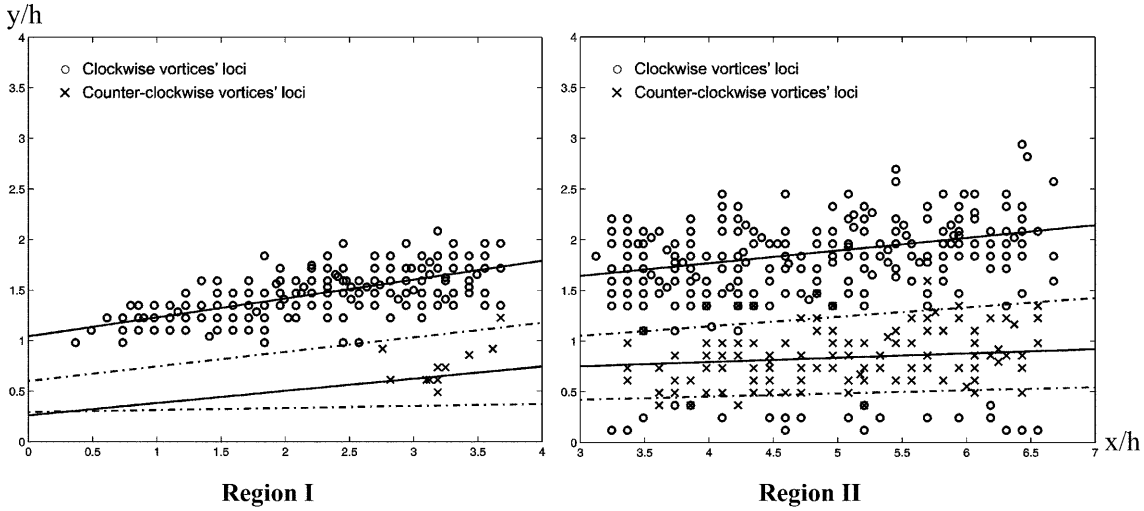

Fig. 13. Loci of vortex structures in the center streamwise/wall-normal plane. *Circles* represent the hairpin vortex heads and *crosses* the reverse vortices, concentrated in different zones, *solid lines* are linear regressions of the vortex loci, and they are found to match with the linear regressions of the inflection points in the mean velocity profiles shown in Fig. 14, *dashed lines* at the borders of the zones represent traces of the indent points on the mean velocity profiles shown in Fig. 14

time series of instantaneous PIV measurements (velocity fields superimposed with vorticity fields) in region II in the center streamwise/wall-normal plane, with the reference-frame velocity set at 56% U_0. The head of primary hairpin A shed from the tab entered the viewing window in Fig. 8a. Subsequently in Fig. 8b, a new vortex R with opposite-sign vorticity ($\omega_z > 0$ or counter-clockwise rotation) was formed below A. In Fig. 8c, another vortex S with same-sign vorticity as A ($\omega_z < 0$) was generated in the wake of the primary hairpin A. This new vortex S is identified as a secondary hairpin vortex for reasons to be discussed later. In Fig. 8d, the loci of the parent hairpin vortex A, secondary hairpin S, and the next primary hairpin vortex B, form an inverse triangle often observed from our PIV data. The secondary hairpin vortex S advected slower than the primary hairpin heads, apparently due to the deceleration by its preceding hairpin vortex A, and its trailing hairpin vortex B. It was finally caught up by the trailing vortex B. These two co-rotating vortices quickly approached each other (Fig. 8e) and merged through a pairing process in (Fig. 8f), where they were followed by another hairpin vortex head, C. The amalgamation between a secondary hairpin vortex head and a primary hairpin vortex head was also observed by Acarlar and Smith (1987a, b) in their flow visualization study of hairpin vortices generated by a half-hemisphere or fluid injection in a laminar boundary layer. Similar to what they observed, a secondary hairpin vortex head often merged with its trailing primary hairpin rather than the preceding primary hairpin vortex in this flow. Although this merging process could be very complicated in three dimensions, in the central two-dimensional plane it appeared similar to a classical vortex pairing process.

3.4.1
Generation of secondary hairpin vortex

From observations of the PIV data, a speculative explanation for the generation of the same-sign secondary hairpin vortex in the tab flow is attempted here based on the vortex-induced boundary-layer separation concept proposed by Peridier et al. (1991a, b). The induction by both the head and the legs of a primary hairpin vortex A led to a localized breakdown of the boundary layer and lift-up or ejection of the surface fluid away from the wall, upstream of the hairpin head. The ejection, being in the second quadrant, is commonly called Q2 ejection. This low-speed fluid then interacted with the high-speed fluid incoming from the top to produce an unstable shear layer. This shear layer subsequently rolled up into a distinct secondary hairpin vortex S with $\omega_z < 0$. This explanation appears to be consistent with the PIV measurements shown in Fig. 8. It also appears to be consistent with observations from the PIV measurements in the x–z plane shown in Fig. 9. In the x–z plane, the interaction of the ejected low-speed fluid between the hairpin legs and the incoming high-speed fluid produced two unstable shear layers that rolled up to form two new legs. This hairpin regeneration process, when occurring in the turbulent wall layer, has been referred to as the viscous–inviscid interaction (Peridier et al. 1991a, b; Smith et al. 1991; Smith and Walker 1995). Smith et al. (1991) described the mechanism as localized unsteady separation. The current PIV measurements provided evidence to support such a model. Other features of the tab wake in the x–z plane will be discussed in Sect. 3.6.

In Fig. 8, the identified primary hairpin vortices A, B, C and the vortex before A were regularly spaced at an average spacing of 3.1 cm. They were periodically shed from the tab at a frequency of 3.9 Hz with a Strouhal number of 0.3. Vortex S was irregularly spaced with its neighboring vortices (A and B). This is reasonable since it was not shed from the tab; rather, it was a secondary vortex.

In most cases when a secondary hairpin vortex was generated, the Q2 ejection was very strong and uninterrupted following the parent hairpin. However, in the particular example of Fig. 8, the reverse vortex R seemed to get in the way in Fig. 8b, but in Fig. 8c it was clear that

that the Q2 ejection continued further upstream. It must be pointed out that it was not very common for vortices S and R to appear in the same PIV picture. At this time, we do not fully understand what specific conditions warrant the generation of secondary hairpin vortices such as S, and of reverse vortices such as R.

3.4.2
Generation of reverse vortex

The spontaneous generation of opposite-sign vortices, such as vortex R in Fig. 8, of reverse rotation with respect to the primary hairpin vortex, occurred frequently in the tab wake. It appeared to be a result of the interaction between the decelerated fluid immediately below the parent hairpin head and the typically faster flow further underneath. From the experiment, we noticed that at the very least a primary vortex head had to be sufficiently strong and far away from the wall to generate a reverse vortex.

The reverse vortices were unmistakably present in the PIV measurements in the x–y plane. They appeared as if they were secondary hairpin "heads", with opposite-sign vorticity, located in a zone below the primary hairpin vortices. However, since we did not clearly see in the horizontal measurements (x–z plane) any convincing evidence of secondary hairpin "legs" with rotations opposite to the normal hairpin legs, we do not know the three-dimensional shape of the reverse vortices, and hence we would not speculate on whether they were hairpin shaped.

3.5
Spatial segregation of vortices of opposite signs

To further examine the evolution of the vortex structures in the tab wake, we plot the loci of all vortices identified in the PIV measurements in the streamwise/wall-normal planes (Fig. 13). Circles and crosses represent the loci of the vortices with negative vorticity (clockwise rotation) and positive vorticity (counter-clockwise rotation), respectively. From the discussions above, we know that the vortices with negative vorticity were the heads of hairpin-like vortex structures (primary and secondary combined), and vortices with positive vorticity were the reverse vortices. These plots demonstrate that vortices of different signs had a high degree of spatial segregation. The reverse vortices were restrained in a zone just underneath the hairpin head zone. Below the zone of reverse vortices, we again find vortices of the clockwise rotation, which were perhaps tertiary vortices.

The two solid lines in region I and region 2 are the linear regressions of vortex loci in Fig. 13. It is worthwhile to point out that these regression lines match very well with the regression lines of the inflectional points ($\mathrm{d}^2U/\mathrm{d}y^2 = 0$) calculated from the mean velocity profiles shown in Fig. 14a, b. The comparison of the regression equations is given in Table 1. The two dashed lines in Fig. 13, visually separating vortices of opposite signs, represent the traces of the indent points ($\mathrm{d}U/\mathrm{d}y = 0$) calculated from the mean velocity profiles in Fig. 14a, b. A detailed discussion of the mean profiles is given in Sect. 3.7. The PIV data shows that 98% of the hairpin vortices and 99% of the reverse vortices were confined in their respective segregated regions.

The high degree of segregation of vortices with different signs in the x–y plane may be attributed to the shear layers induced by the preceding vortices with the same sign. Since a hairpin vortex accelerates the fluid above it and retards the flow below it, a shear layer with negative vorticity is developed after the hairpin has passed. This shear layer, which can be seen from the mean profiles in Fig. 14, can sustain clockwise-rotating vortices (hairpins), but would damp the counter-clockwise vortices (reverse vortices). Therefore, had a counter-clockwise vortex been pumped into this shear layer, it would have diffused quickly, and thus would not be able to maintain its identity in the hairpin dominant region. By the same token, a hairpin vortex cannot survive in the reverse vortex zone.

3.6
Observations in the streamwise/spanwise plane

On a horizontal plane $1.46h$ from the wall, PIV measurements were taken in two partially overlapping regions (II and III) of size 5×5 cm ($3.8h \times 3.8h$) starting 4 cm downstream of the tab tip. Figure 9 shows a typical time series of instantaneous velocity fields measured in region II superimposed with their vorticity fields. The velocity fields are viewed with 50% U_0 subtracted. Two successive pairs of counter-rotating vortex structures (denoted as A and B) are visualized. They were aligned roughly along z, with coarsely circular motions. Consistent with the three-dimensional topology of the hairpin vortex, each pair of vortices in Fig. 9 was identified as the cross-section of the pair of legs of a hairpin vortex, as sketched in Fig. 6b. Facing downstream, the top one was the left leg (L) and the bottom one, the right leg (R). From the PIV measurements, the left and right legs of a hairpin vortex did not have to be symmetric about the center plane. Imaginary lines connecting the centers of A–L and A–R and the centers of B–L and B–L were obviously tilted from the z direction. Examining a large number of PIV pictures of the flow on the x–z planes, we have found that most of the vortex pairs were tilted. The x–z tilting angles of the vortex pairs were non-uniform and could be in either direction. The spacing between the two legs also varied, and the vortex pairs could be laterally shifted towards $+z$ or $-z$ by various amounts. The tilting and staggering, as well as unequal sizes and shapes of the two vortex-leg cores, suggests a type of asymmetry of the hairpin vortices. This is another departure from the conceptual model proposed by Gretta and Smith (1993) shown in Fig. 2. This asymmetry might be attributed to a lateral shedding-type of behavior. However, the large number of PIV pictures containing adjacent hairpin vortices on the x–z plane did not display any alternating lateral shedding pattern. The spanwise variations appeared to be rather irregular at this Reynolds number ($Re_h = 2{,}080$). Elavaransn and Meng (2000) have shown that at $Re_h < 1{,}000$, the hairpin legs were much more symmetric about the tab centerline.

3.6.1
Secondary hairpin vortex legs

We further notice in Fig. 9a that low-speed fluid was accumulated between each pair of hairpin legs. This is consistent with the Q2 ejection seen in the x–y plane by the

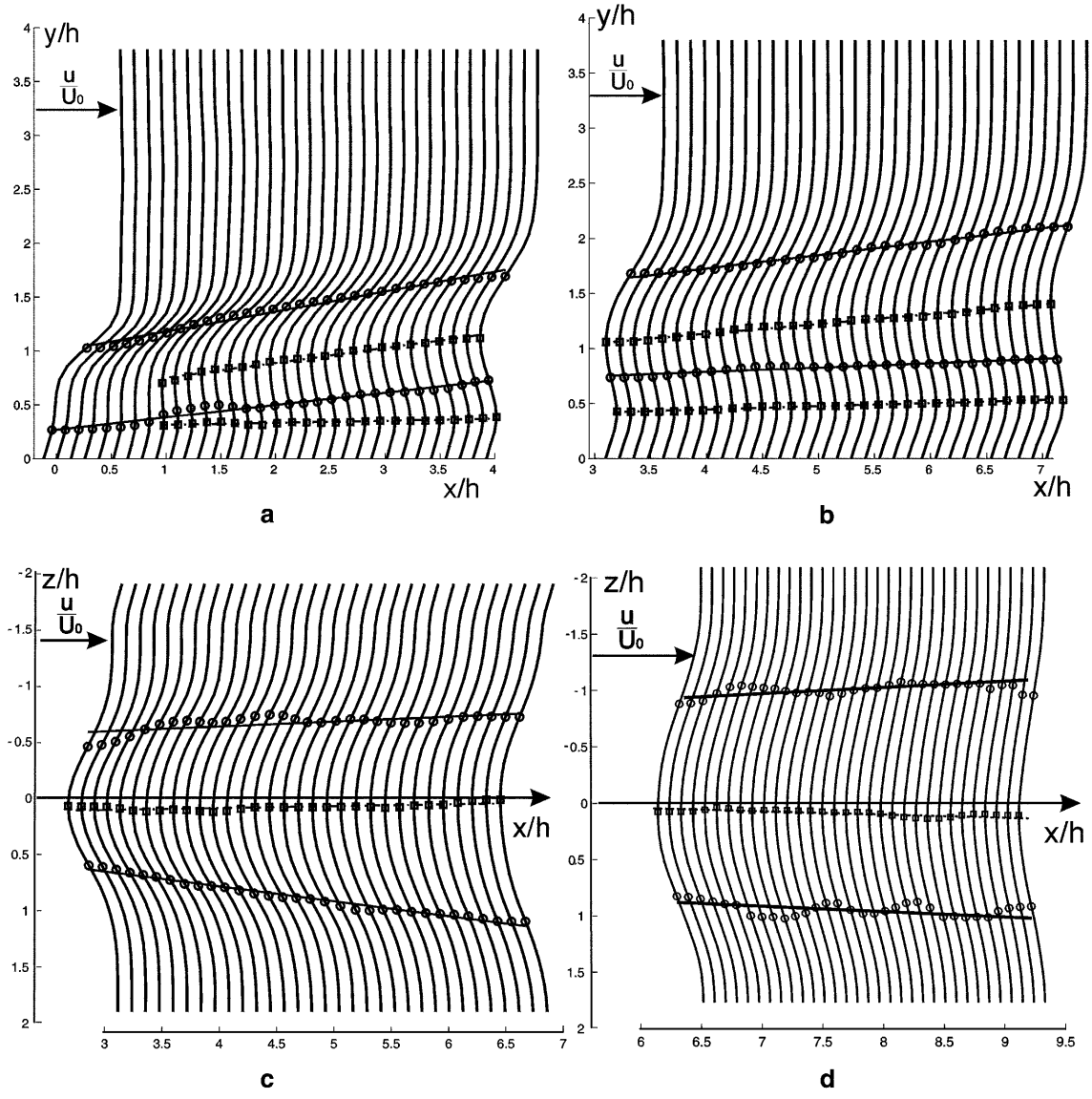

Fig. 14a–d. Mean profiles of streamwise velocity. O inflection points, □ indent points, *straight lines* linear regression. **a** $U(y)$ in region I of the x–y plane, **b** $U(y)$ in region II of the x–y plane, **c** $U(z)$ in region II of the x–z plane, **d** $U(z)$ in region III of the x–z plane

Table 1. Comparison of regressions for vortex loci (from Fig. 13) and mean velocity inflectional points (from Fig. 14)

	Regression equation for vortex loci	Regression equation for inflectional points on mean velocity profiles
Upper solid line in region I	$y = 0.1849x + 1.0579$	$y = 0.1866x + 1.0433$
Upper solid line in region II	$y = 0.1143x + 1.2964$	$y = 0.1250x + 1.2681$
Lower solid line in region I	$y = 0.1301x + 0.2507$	$y = 0.1208x + 0.2616$
Lower solid line in region II	$y = 0.0419x + 0.6266$	$y = 0.0675x + 0.6231$

two hairpin legs. Combining the analyses of both x–y and x–z instantaneous velocity fields, we can imagine a finite strip of low-speed fluid being lifted up between the two hairpin legs. The fluid outside the hairpin legs was accelerated due to induction of the legs. In Fig. 9b, the strip of low-speed fluid between the legs of vortex B extended upstream, and when it interfaced with the high-speed flow on both sides, new shear layers were generated with the same-sign vorticities as those of B–L and B–R. In the next two instants shown in Fig. 9c, d, these two shear layers developed into a pair of new vortices, S–L and S–R. Vortices S–L and S–R were identified as the left and right legs of a newborn secondary hairpin vortex, S. From the PIV measurements it is speculated that the legs of a secondary hairpin vortex were also generated through a localized unsteady boundary-layer separation. Due to the induction of a parent hairpin vortex, the near-wall, viscous fluid broke down from the surface and was ejected backward and upward. This ejected low-speed fluid interacted with the high-speed fluid through a viscous–inviscid interaction

(Peridier et al. 1991a, b). This interaction was a three-dimensional process. In the spanwise direction, it generated a secondary hairpin vortex head, and in the streamwise direction, it generated the secondary hairpin legs.

3.7
Turbulence statistics

From the above analyses, the instantaneous PIV pictures have revealed very active coherent structure dynamics in the mixing tab wake. On the other hand, turbulence statistics (such as mean velocity profiles, Reynolds shear stresses, turbulent kinetic energy, and its dissipation rate) can reveal the characteristics of this flow from a Reynolds-average point of view. These statistical quantities may be more familiar to the process designer in assessing the transport effects. Furthermore, correlation of the dynamical events of the coherent structures with the turbulence statistics can reveal the effects of vortex dynamics on the mean flow characteristics. From a large number of PIV measurement realizations taken in short time sequences that were independent from each other, we obtained time-averaged statistics, which roughly approximated the turbulence statistics.

3.7.1
Mean velocity profiles

Mean profiles of the streamwise velocity $U(y)$ as a function of x and y and $U(z)$ as a function of x and z were obtained by averaging instantaneous velocities from PIV measurements. Figure 14 shows mean velocity profiles of two partially overlapping measurement regions (I and II) in the streamwise/wall-normal plane (x–y) and two partially overlapping regions (II and III) in the streamwise/spanwise plane (x–z). The profiles were fitted by high-order polynomial curves. The $U(y)$ profiles in Fig. 14a, b agree with the mean profiles measured by Gretta and Smith (1993) using hot-film anemometry including the inflectional characteristics.

Inflection points (where $d^2U/dy^2 = 0$ or $d^2U/dz^2 = 0$) and indent points (where $dU/dy = 0$ or $dU/dz = 0$) were calculated from the fitted mean velocity profiles from the PIV measurements. In Fig. 14a, b, each $U(y)$ profile in region I and region II exhibits two inflection points. Two lines from linear regression of the inflection points have been fitted to trace the development of the inflections. From $x \approx 1h$ on, two indent points, one below each inflection point, also developed on these profiles. The indents reached a maximum amount at $x \approx 4h$, after which the profiles started to flatten out and gradually recovered to the normal channel flow profile. The inclination angles of the inflection and indent points are given in Table 2.

Table 2. Inclination angles of the inflection point lines and indent point lines on the mean velocity profile $U(y)$ shown in Fig. 14a, b

	Region I	Region II
Upper inflection	10.6°	6.9°
Upper indent	8.2°	5.3°
Lower inflection	6.9°	3°
Lower indent	1.2°	1.8°

The mean velocity profiles shown in Fig. 14a, b contain clear imprints of the hairpin vortex heads (upper inflections in the profile) and imprints of the reverse vortices (lower inflections). As shown earlier in Table 1, the upper and lower inflection point lines coincide with the average path of the passing hairpin vortex heads and the reverse vortex heads, respectively. The rising inflection points indicate the time-averaged effect of the rise of hairpin vortices with the downstream distance. The different inclination angles in regions I and II reflect different vortex dynamics in these two regions. These profiles also support the observation that hairpin vortex heads (clockwise rotation) and reverse vortex vortices (counter-clockwise rotation) were located in different zones along the wall-normal direction. The flattening of the profiles at large downstream distances suggests a weakening presence of the vortices.

Figure 14c, d shows the $U(z)$ profiles in measurement regions II and III on the horizontal plane, $1.46h$ from the bottom wall. Although this plane is above the tab, the mean flow shows a distinct "wake" or low-speed wake region near the centerline of the tab. From Fig. 13 we see that at $x = 3$, where region II starts, the hairpin heads were already at an average height of $1.7h$, and hence we expect that the horizontal imaging plane (x–z) at $1.46h$ would cut through hairpin legs. Each velocity profile contains two inflection points, whose distances from the centerline increases with x in region II. Two straight lines from linear regressions were fit to the inflection points in region II. In region III, some intermittent fluctuations of the traces can be noticed. Relating to the instantaneous velocity fields, it can be inferred that the inflection points were imprints of the two hairpin vortex legs. It can also be inferred that the centerline fluid deceleration in the mean profile was caused by the common-backward induction of the legs and was a manifestation of the low-speed strip. This explanation is illustrated in Fig. 15. At $x = 3.2h$ the curvature of $U(z)$ profile reaches its peak value (most severe deceleration). Thereafter, the defects in velocity profiles gradually flatten out, approaching the free-stream velocity. Evidently, the recovered free-stream velocity profile maintained the two-dimensionality of the channel flow in the test region.

3.7.2
Reynolds stresses

Reynolds shear stresses, $<u'v'>$ and $<u'w'>$ were computed from the PIV data in the measurement regions in the x–y plane and the x–z plane, respectively and were plotted as two-dimensional contour lines in Fig. 16. The Reynolds stress $<u'v'>$ shown in Fig. 16a, b can be visually correlated with the inflection points in Fig. 14a, b. Furthermore, the core of the negative Reynolds stress region (with the Reynolds stress ≤ -0.0107 when normalized with the square of the free-stream velocity, i.e., level 3 in Fig. 16a, b) can be correlated with the upper inflection point line, which represents the statistical path of hairpin vortex heads. This suggests that hairpin vortices were responsible for the negative Reynolds stress in the x–y plane, which indicates strong Q2 and Q4 momentum transport between free-stream and near-wall

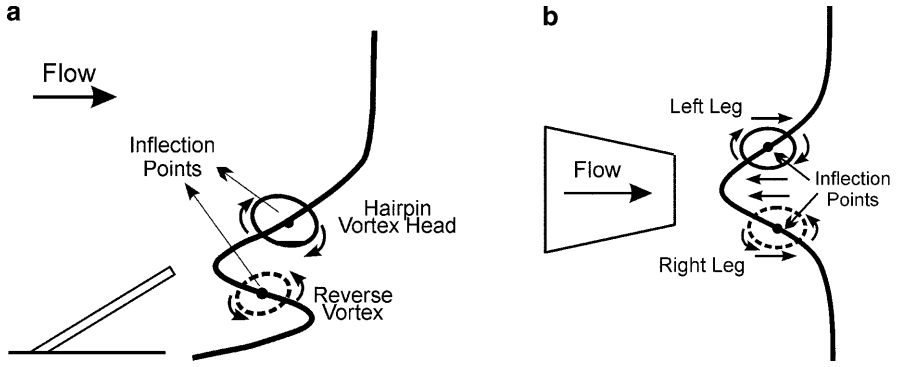

Fig. 15a, b. Illustration of hairpin vortex and reverse vortex imprints on the mean velocity profiles shown in Fig. 13. **a** $U(y)$ in the x–y plane and **b** $U(z)$ in the x–z plane

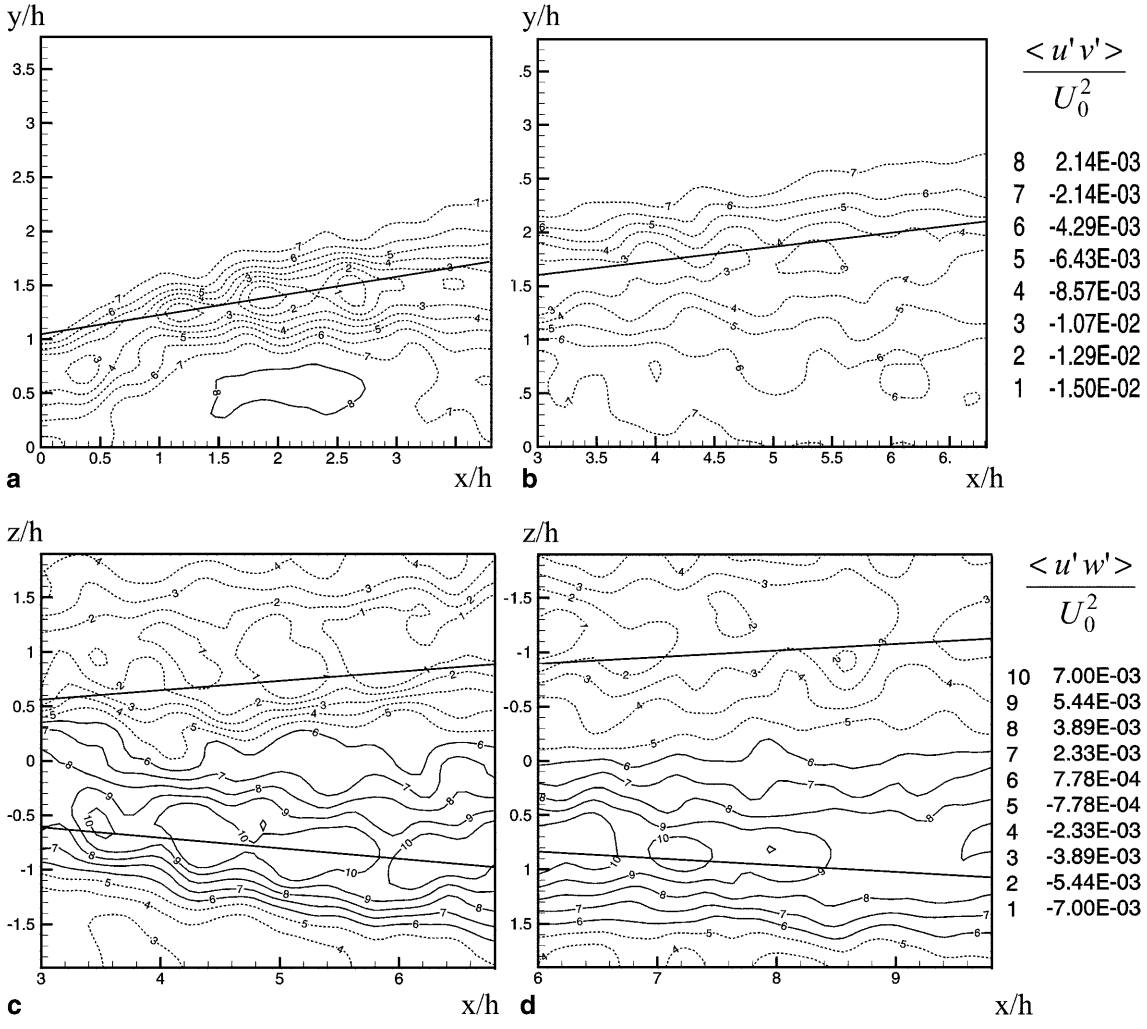

Fig. 16a–d. Reynolds shear stresses measured in the x–y and x–z planes. The *solid straight lines* are linear regressions of the inflection points in the mean velocity profiles shown in Fig. 13. *Dashed lines* negative; *solid lines* positive. **a** $<u'v'>$in the x–y plane in region I, **b** $<u'v'>$in the x–y plane in region II, **c** $<u'w'>$in the x–z plane in region II, **d** $<u'w'>$in the x–z plane in region III

fluids. Figure 16c, d shows the distribution of Reynolds stress in regions II and III in the streamwise/spanwise (x–z) plane. The cores of the regions with strong negative and positive Reynolds stresses, again match very well with their corresponding inflection lines in Fig. 14c, d. This strongly suggests that hairpin legs caused the formation of these two strong Reynolds stress regions in the x–z plane.

3.7.3 Turbulence dissipation rate

The dissipation rate of turbulent kinetic energy is an important indication of turbulent mixing at small scales. A partial representation of ε was estimated from the PIV measurements using a large-eddy PIV method proposed by Sheng et al. (2000). Under the dynamic equilibrium assumption, the turbulence dissipation rate ε can be approx-

imated by the sub-grid scale (SGS) energy flux ε_{SGS} at the cut-off scale corresponding to the PIV spatial resolution:

$$\varepsilon \approx \langle \varepsilon_{SGS} \rangle = -2\langle \tau_{ij}\bar{S}_{ij} \rangle$$

The SGS flux ε_{SGS} can be obtained from the mean strain-rate tensors, $\bar{S}_{ij}$, computed from the PIV-measured (thus "resolved") velocity fields and the modeled SGS stress, τ_{ij}. In the current calculation, the Smagorinsky eddy–viscosity model (Smagorinsky 1963) was employed to calculate the SGS stress τ_{ij}:

$$\tau_{ij} = -C_s^2 \Delta^2 |\bar{S}| \bar{S}_{ij} \ ,$$

where $C_s = 0.17$ is the Smagorinsky constant, $\Delta = 1$ mm is the spatial filter size, corresponding to the spatial resolution of the PIV measurements, and $|\bar{S}|$ is defined as $\left|\sqrt{2(S_{ij}S_{ji})}\right|$. In the tab center plane, $\frac{\partial u}{\partial x}, \frac{\partial u}{\partial y}, \frac{\partial v}{\partial x}$, and $\frac{\partial v}{\partial y}$ can be calculated directly from PIV data, and $\frac{\partial w}{\partial z}$ can be derived from the above terms by applying the continuity equation for incompressible flow. The rest of the terms in the strain-rate tensor $\left(\frac{\partial w}{\partial x}, \frac{\partial w}{\partial y}, \frac{\partial u}{\partial z}, \frac{\partial v}{\partial z}\right)$ were unavailable from our two-dimensional PIV measurements. However, since the flow along the tab center plane was roughly symmetric in the statistical sense, the contribution from the missing terms was insignificant. Figure 17 shows distributions of the estimated turbulence dissipation rate in regions I and II on the center x–y plane.

From the plot, an area with large dissipation rate (defined as $\varepsilon > 0.00015$ m^2/s^3) extends vertically from the wall to a height of 1.2 h just after the tab, and from the wall to 2 h at $x/h \approx 5$. Through the spatial integration of energy dissipated within the aforementioned area normalized by the total energy dissipated (over a unit time), it was found that 80% of total turbulent kinetic energy was dissipated in this region. Hence, it can be suggested that high-efficiency mixing at small scales was achieved only within a certain region ($x/h < 6.0$, $y/h < 2.0$) behind the tab.

3.7.4 Mixing effectiveness

Several things can be learned from the statistics results in terms of the mixing effectiveness of the HEV mixer. In this discussion, we relate Reynolds stress as to macro mixing (i.e., mixing of fluid at the energy-containing or large-scale eddies) and turbulent kinetic energy dissipation rate to micro mixing (i.e., mixing at the dissipative fine scales). Macro mixing is directly relevant to applications such as blending and is required before micro mixing can occur massively. Micro mixing directly affects molecular diffusion and thus is important for chemical reactions. From the statistics based on PIV measurements of the mixing tab flow:

1. It is observed that the Reynolds stress distribution coincides with the passage of the hairpin vortices, and thus the hairpin vortices are mostly responsible for macro mixing. The hairpin vortex size is on the order of the size of the tab, and the influence of the hairpin vortices spans the tab wake in both the vertical and the horizontal directions. Hence, to generate macro mixing in a larger region in an HEV mixer while keeping the same number of tab elements, a larger tab size should be used.
2. For a single tab element, the macro-mixed region gets wider with the downstream distance and persists as long as the hairpin vortices persist (up to 12 h observed in this experiment), while the mixing intensity (loosely reflected by the magnitude of Reynolds stress) gets weaker with the downstream distance. To keep the mixing intensity above a certain level, multiple tab elements should be added downstream.
3. In an HEV mixer, the strongest vertical fluid transport in the tab center plane is in the regions where hairpin vortex heads are, and the transport is mainly along the Q2/Q4 directions (see Fig. 6a for definition); the strongest horizontal fluid transport is in the regions

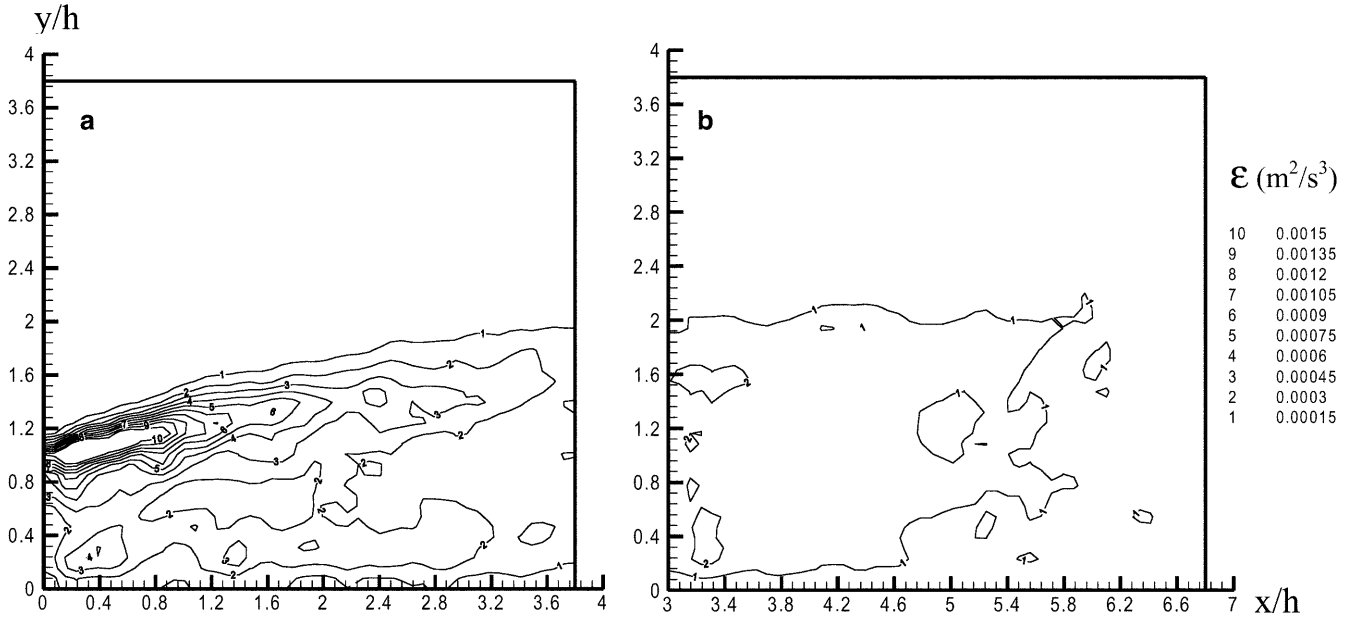

Fig. 17a, b. Turbulent dissipation rate measured in the x–y plane in **a** region I and **b** region II

where hairpin vortex legs are. The left hairpin vortex legs perform the Q2/Q4 transport while the right legs perform the Q1/Q3 transport in the horizontal plane.

4. It is observed that the dissipation rate is the strongest about one tab height downstream and decreases faster with the downstream distance than the Reynolds stress. It implies that efficient micro mixing is maintained within a shorter distance in the tab wake than efficient macro mixing. Hence, an HEV mixer that is used primarily as a chemical reactor should contain more densely spaced tab elements than an HEV mixer that is used primarily as a blender.
5. It is also observed that the dissipation rate does not spread as widely cross-streamwise as the Reynolds stress distribution. It suggests that the tab performs macro mixing in a wider cross-stream region than it performs micro mixing.

Our final remark is that hairpin vortex structures are highly three-dimensional. Their dynamics, and their interaction with each other as well as with other vortical structures, cannot be fully understood without fully resolved three-dimensional velocity field measurements. The two-dimensional PIV measurements only provide two-dimensional cuts of the complex three-dimensional physical processes. It is worthwhile to mention that holographic PIV has been applied to the mixing tab flow to obtain three-dimensional snapshots of the velocity and vorticity fields with rather encouraging initial results (Pu and Meng 2000). Such a technique holds great promise to improve our understanding of hairpin vortex dynamics and relevant industrial problems.

4
Concluding remarks

Time-series PIV measurements showed that hairpin vortices were shed periodically from a single mixing tab and grew in both height and scale with the increasing downstream distance. Secondary hairpin vortices were observed in the mid-field region in both the x–y and x–z planes. The PIV results were consistent with the vortex-induced boundary-layer separation concept for the regeneration of hairpin vortices. The pairing process of a secondary hairpin vortex and its trailing primary hairpin vortex was also clearly captured. Experimental evidence shows that the vortex-induced ejection of the near-wall viscous fluid to the immediate upstream is important to the dynamics of hairpin vortices. It can increase the strength of the hairpin vortices in the near tab region and cause generation of secondary hairpin vortices further downstream when the hairpin heads are farther away from the wall. Furthermore, a new type of offspring vortex structures with opposite-sign vorticity has been found in the tab wake in the streamwise/wall-normal plane. These reverse vortices were generated below their primary hairpin vortices, seemingly through the roll-up of reversed shear layers that were produced by the deceleration of fluid underneath the primary hairpin vortices. The reverse vortices were spatially segregated from the hairpin vortex heads. Both hairpin vortices and reverse vortices left clear footprints on the mean velocity profiles as opposite inflections. Hairpin vortices were also seen to correlate well with Reynolds stresses, indicating that these large-scale structures are responsible for the macro mixing in the tab wake.

References

Acarlar MS; Smith CR (1987a) A study of hairpin vortices in a laminar boundary layer, Part 1. Hairpin vortices generated by a hemisphere protuberance. J Fluid Mech 175: 1–41

Acarlar MS; Smith CR (1987b) A study of hairpin vortices in a laminar boundary layer, Part 2. Hairpin vortices generated by fluid injection. J Fluid Mech 175: 43–83

Chong MS; Perry AE; Cantwell BJ (1990) A general classification of three-dimensional flow fields. Phys Fluids A2: 765–777

Elavarasan R; Meng H (2000) Flow visualization study of role of coherent structures in a tab wake. Fluid Dyn Res 27: 183–197

Gretta WJ; Smith CR (1993) The flow structure and statistics of a passive mixing tab. J Fluid Eng 115: 255–263

Haidari AH; Smith CR (1994) The generation and regeneration of single hairpin vortices. J Fluid Mech 277: 135–161

Head MR; Bandyopadhyay P (1981) New aspect of turbulent boundary-layer structure. J Fluid Mech 107: 297–337

Jeong J; Hussain F (1993) On the identification of a vortex. J Fluid Mech 285: 69–94

Keane RD; Adrian RJ (1992) Theory of cross-correlation analysis of PIV images. Appl Sci Res 49: 191

Kim J (1987) Evolution of a vortical structure associated with the bursting event in a channel flow. In: Durst F; Launder BE; Lumley JL; Schmidt FW; Whitelaw JH (eds) Turbulent Shear Flows 5. Springer, Berlin Heidelberg New York, pp 221–233

Malkiel E; Levinski V; Cohen J (1999) The evolution of localized vortex disturbance in external shear flows, Part 2: Comparison with experiments in rotating flows. J Fluid Mech 379: 351–380

Meinhart CD; Adrian RJ (1995) On the existence of uniform momentum zones in a turbulent boundary layer. Phys Fluids 7(4): 694–696

Moin P; Leonard A; Kim J (1986) Evolution of curved vortex filament into a vortex ring. Phys Fluids 29(4): 955–963

Peridier VJ; Smith FT; Walker JDA (1991a) Vortex-induced boundary-layer separation. Part 1: The unsteady limit problem $Re \rightarrow \infty$. J Fluid Mech 232: 99–131

Peridier VJ; Smith FT; Walker JDA (1991b) Vortex-induced boundary-layer separation. Part 2: Unsteady interacting boundary layer theory. J Fluid Mech 232: 133–165

Perry AE; Chong MS (1982) On the mechanism of wall turbulence. J Fluid Mech 119: 173

Pu Y; Meng H (2000) An advanced off-axis holographic particle image velocimetry system. Exp Fluids 29(2): 184–197

Raffel M; Willert CE; Kompenhans J (1998) Particle image velocimetry. Springer, Berlin Heidelberg New York

Robinson SK (1990) Kinematics of turbulent boundary layer structures. PhD thesis, Stanford University, Stanford, Calif

Robinson SK (1991) Coherent motions in turbulent boundary layers. Annu Rev Fluid Mech 23: 601–639

Schoppa W; Hussain F (1997) Genesis and dynamics of coherent structures in near-wall turbulence: A new look. In: Panton R (ed), Self-sustaining mechanisms of wall turbulence. Computational Mechanics Publications

Sheng J; Meng H; Fox RO (2000) A large eddy PIV method for turbulence dissipation rate estimation. Chem Eng Sci 55: 4423–4434

Smagorisky J (1963) General circulation experiments with the primitive equation I the basic experiment. Monthly Weather Rev 91: 99–164

Smith CR; Walker JDA (1995) Turbulent wall-layer vortices. In: Green S (ed) Fluid vortices, chap VI. Kluwer, Dordrecht, pp 235–290

Smith CR; Walker JDA; Haidari AH; Sobrun U (1991) On the dynamics of near-wall turbulence. Phil Trans R Soc Lond A336: 131–175

Spalding DB (1961) A single formula for the "law of the wall". J Appl Mech 28: 455–457

Theodorsen T (1952) Mechanism of turbulence. In Proceedings of the 2nd Midwestern Conference on Fluid Mechanics, Ohio State University, Columbus, Ohio

Zhou J; Adrian RJ; Balachandar S; Kendall TM (1999) Mechanisms for generating coherent packets of hairpin vortices in channel flow. J Fluid Mech 387: 353–396

Zhou J; Meinhart CD; Balachandar S; Adrian RJ (1997) Formation of coherent hairpin packets in wall turbulence. In: Panton RL (ed) Self-sustaining mechanisms of wall turbulence. Computational Mechanics Publications